LEGI
LABORATOIRE DES ECOULEMENTS GÉOPHYSIQUES ET INDUSTRIELS

OSUG
Observatoire des Sciences de l'Univers de Grenoble

UPMC
PARIS UNIVERSITAS

M2R Internship

Oceanic Circulation and Dynamical Processes Around the Reykjanes Ridge. Numerical Simulations and Laboratory Experiments

---

Supervised by Achim Wirth and Jan-Bert Flor

LEGI Laboratory - Team MEIGE

Thibault Jougla

M2R OACOS - Paris

Contents

Chapter 1

Acknowledgement

I would like to thank the LEGI laboratory for the welcome during this project, internship and PhD students for all the moments spend together. I would like also to thank the computer developers Olivier De Marchi and Cyrille Bonamy for the help they give me on numerical problems. And, I would like to thank my two internship supervisors, Achim Wirth and Jan-Bert Flor for the help, and explanations they have given me with pedagogy, simplicity and kindness and for all the moments spend together.

Chapter 2

Abstract

The Reykjanes ridge is situated between the Irminger basin and the Iceland basin, at the intersection of different flows determining the global ocean circulation. The flow coming from the Faroe Bank channel turns around the ridge. The aim of this project is to understand the dynamic processes around the ridge. To the best of our knowledge idealized studies on the circulation around sloping ridges, focusing on meso- and sub-meso-scale structures are scant.
For this study, idealized numerical simulations and qualitative laboratory experiments have been performed. I used a fine resolution reduced gravity rotating shallow-water model to investigate the oceanic flow around a ridge, which I developed from scratch. After, validation of the ridge configuration for a variety of experiments over extended periods, and laminar to turbulent flows, I analyze the flow behavior around the ridge for the different regimes. In parallel, we have done some laboratory experiments using a novel measuring technique based on optical methods, showing the adequation of this method for studying ridge flows.
For laminar and turbulent flows, while turning around the ridge, coastal waves propagate from the injection to the upwelling areas. For high injection rates the flow is turbulent and shows asymmetry between the two sides of the ridge. For turbulent flows, eddies are released from the ridge front, forming β-plumes. Around the ridge, smaller eddies and filaments emerge from larger scale eddies. To investigate the dynamics, a scale analysis, Hovmoller diagrams, and age tracers are used.
The eddies flow arriving to the ridge is transformed to a succession of β-plumes. The speed of eddies increases approaching the north-eastern boundary.

Chapter 3

Introduction

3.1 General aspects, Atlantic circulation

The Meridional Overturning Circulation (MOC) is a global oceanic circulation influenced by salinity and temperature variations. The principal factors that have an impact on the MOC are the wind forcing, the heat fluxes, the fresh water fluxes and the vertical mixing.
In the tropical area the water at the surface becomes hotter and saltier (see equation(3.1)). The hot and salty water in the upper ocean from the tropical area is moving northward, bringing with it heat from low latitudes at high latitudes. The heat is released to the atmosphere. A famous example is the Gulf Stream, which carries warm water from the Caribbean sea to Europe. Thanks to the Gulf Stream some polar areas, like the Svalbard islands, have temperatures around $-6°C$ at a latitude close to $78°N$. In the southern hemisphere, this latitude corresponds to the middle of the Antarctic continent. Due to convection, at very high latitudes, cold and dense water sinks and creates intermediate and deep waters, especially the North Atlantic Deep Water (NADW). This downwelling appears at some very specific areas and at some specific moments. Cold and dense water is transported to the tropics where it wells up to the surface, and the cycle starts again. The timescale of this cycle is $1000 - 1500$ years. This heat transport with a long timescale can have an important impact on our climate.

$$\rho = \rho_0(1 - \alpha\Delta T + \beta\Delta S + \gamma\Delta p) \tag{3.1}$$

3.2 Reykjanes Ridge

This project is inspired by the deep circulation in the north Atlantic area, around the Reykjanes ridge. The topography of this area is characterized by different ridges and basins. The mid Atlantic ridge separates the North and South-American plates from the Eurasian and the African plates, and emerges at some points in the form of islands, like the Azores, Saint Helena and Iceland for instance. The ridge increasing in height of the ocean from the bottom to Iceland is called the Reykjanes ridge and its influence on the oceanic circulation is the topic of this project. The Reykjanes ridge is tilted of $-55°$ with the north-south axis. More or less perpendicularly of this ridge, extends the Greenland-Scotland ridge. Together they define two basins, the Irminger basin West of the Reykjanes ridge and South of the Greenland-Scotland ridge, and on the other side of the Reykjanes ridge the Iceland basin. Figure 3.1 represents the topography of the north Atlantic ocean, the Iceland and Irminger basins are present on each side of the Reykjanes ridge. The Reykjanes ridge is placed at a crossroad of many flows: hot and salty tropical water, the North Atlantic current, cold and less salty sub-polar water and the Iceland-Scotland Overflow

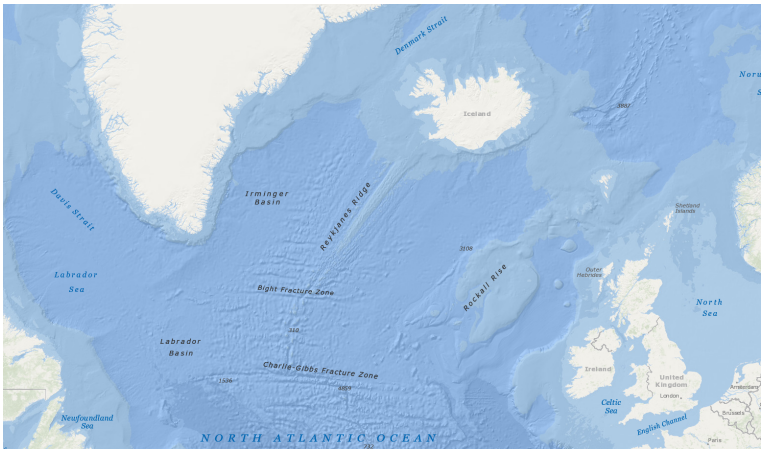

Figure 3.1: Topography of the north Atlantic ocean with the presence of the Reykjanes ridge in the south of Iceland, map from ESRI France.

Water. Figure 3.2 represents the major currents of the North Atlantic overturning circulation.

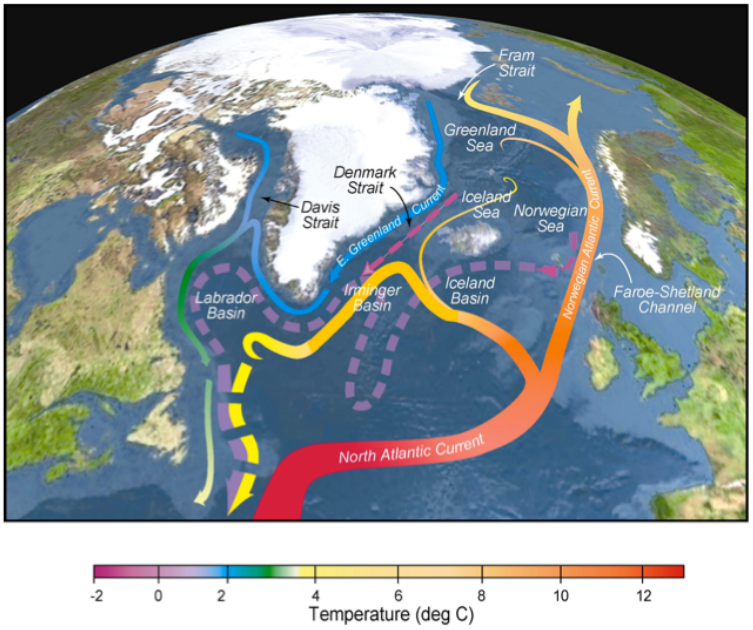

Figure 3.2: North Atlantic overturning circulation. From *Curry and Mauritzen* [2005].

3.3 Ovide project

The aim of the Ovide project is to investigate the sub-polar North Atlantic ocean gyre in the light of the ocean climate variability and interaction with the atmosphere. In situ data has been collected from Portugal to Greenland and near the Reykjanes ridge. In parallel to those observations, the aim here is to study the circulation, the dynamical processes and their non-linear interaction around the Reykjanes ridge. Idealized laboratory experiments and numerical simulations are used.

3.4 Observations

Thanks to satellites the sea surface can be observed and particularly the chlorophyll concentrations can be detected. Figure 3.3 presents the area South of Iceland in 2007. A panel of eddies and filaments between them can be observed due to the variation of the concentration of the phytoplankton and in species composition.

The high resolution of this satellite image, allows the observation of thin filaments in between the eddies, in the Irminger basin

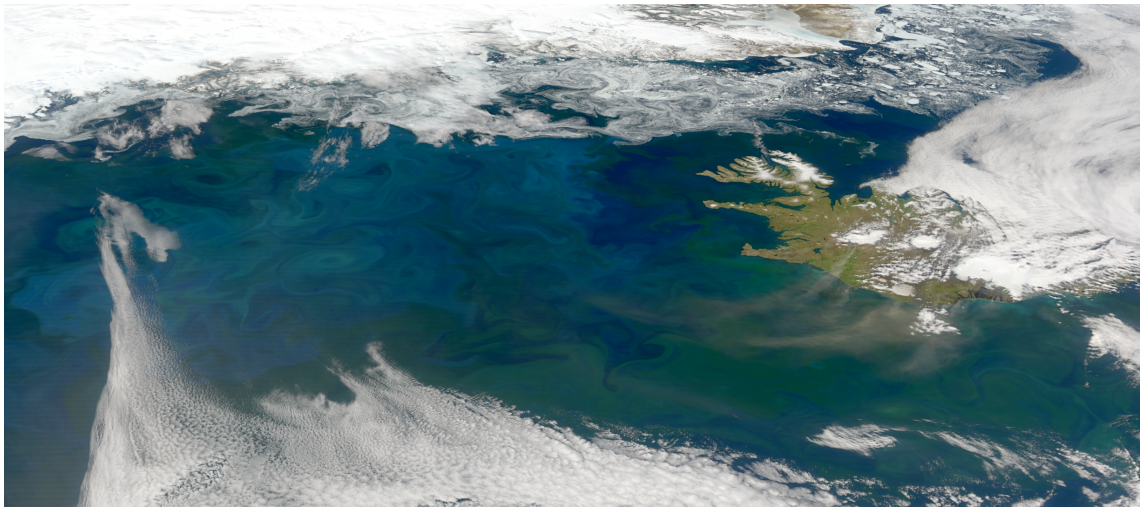

Figure 3.3: Satellite image of the Irminger and Iceland basins. The green colors are due to phytoplankton concentration and other species compositions variations. The sea surface is covered by eddies and filaments. Source: $http://oceancolor.gsfc.nasa.gov/cgi/image_archive.cgi$

Chapter 4

Physical model

The aim of this project is to understand the dynamics of the different flows crossing a ridge in the deep ocean. The ridge here considered is in the North Atlantic ocean, between the Irminger and the Iceland basins. The basin has been taken as a rectangular area of $2,000$ km$*1,000$ km, for two main reasons. First, in reality the Reykjanes ridge is between two basins which can be seen as two squares of size $1,000$ km. The second reason is that water is injected in one side and withdrawn from the other one, to allow the injected flow to be structured, if the flow injected is to close from the ridge, this flow will be unstructured.

The ocean is considered here as a two-layers-fluid with a temperature difference of $5°C$. This difference corresponds to that between the Iceland-Scotland overflow water and the North Atlantic current. A density difference is created. I am mainly concerned with phenomenae in the deep layer, which corresponds to the Iceland-Scotland overflow water. This current arrives from the east (i.e. the Faroe Bank channel) along the edge (i.e. the Greenland-Scotland ridge) to the Reykjanes ridge.

To model this current, water is injected in the north-east side of the basin and withdrawn from the north-west side. Different injected flows have been used to understand the behavior of flows with the ridge (1 Sv, 5 Sv, 10 Sv and 15 Sv). The water is injected in a section of 30 km in the north-east corner and withdrawn in a section of 240 km in the north-west corner. The ridge, long of 1000 km and large of 100 km, is tilted by $-45°$ with the north-south axis. And it is situated at $60°N$, at the south of Iceland. The Greenland-Scotland ridge and the continental shelf hold the water in the basin.

To the best of our knowledge, nobody has study dynamics and processes around a slope ridge. Some studies have been done about topography and vortices, in *Sansón and Van Heijst* [2000] and *Thierry and Morel* [1999] the approach was different and the resolution coarser.

Chapter 5

Mathematical model

The figure represents a longitudinal section of the basin, with the ocean surface and the deep ocean, separated by the thermocline. I only consider the deep ocean. The water is considered homogeneous, with a constant density and with a viscosity $\nu = 50\ \mathrm{m}^2.\mathrm{s}^{-1}$. The latitudes and longitudes are tilted by $-45°$ compare to the x-y axis. The horizontal size of the basin is very high compare to the vertical one. Thus, the rotating shallow water model with reduced gravity is used.

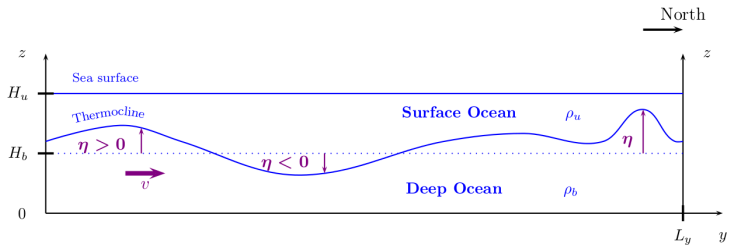

Figure 5.1: Longitudinal representation of the ocean. The thermocline separates the deep ocean from the surface ocean, with a density respectively of ρ_u and ρ_b. I am only interesting in the deep ocean, the elevation of the thermocline is called η, and is positive with and elevation of the height of the ocean. v the longitudinal velocity is positive going northward. And u is positive going eastward. From *Poupart*

5.1 Shallow water model

The main equations used in all parts of fluid dynamics are the Navier-Stockes equations. Even the existence of solutions of these equations is an open problem. I here consider a simplified set of equations adapted to ocean dynamics: the rotating shallow water equations. The shallow water equations describe the behavior of a constant density fluid with vertical dimension smaller than horizontal ones (justifying its name). The mean depth of the Atlantic ocean is around $4,000$ m whereas the horizontal basin length scale is around $5,000$ km. The horizontal length scale is $1,000$ larger than the vertical one. The analogy between the thickness and length of a A4 paper and the ocean depth and horizontal extension is a very good illustration of the aspect ratio. In those conditions the ocean can be considered as 2D, $H \ll Lx, Ly$. The shallow water equations correspond to the depth-integration of the Navier-Stockes equations, i.e. the conservation of momentum and the equation of conservation of mass of a constant density fluid.

$$\frac{\partial u}{\partial t} + u\frac{\partial u}{\partial x} + v\frac{\partial u}{\partial y} - fv = -g'\frac{\partial \eta}{\partial x} + \nu(\frac{\partial^2 u}{\partial x^2} + \frac{\partial^2 u}{\partial y^2}) \tag{5.1}$$

$$\frac{\partial v}{\partial t} + u\frac{\partial v}{\partial x} + v\frac{\partial v}{\partial y} + fu = -g'\frac{\partial \eta}{\partial y} + \nu(\frac{\partial^2 v}{\partial x^2} + \frac{\partial^2 v}{\partial y^2}) \tag{5.2}$$

$$\frac{\partial \eta}{\partial t} + \frac{\partial (h+\eta)u}{\partial x} + \frac{\partial (h+\eta)v}{\partial y} = \kappa(\frac{\partial^2 h}{\partial x^2} + \frac{\partial^2 h}{\partial y^2}) \tag{5.3}$$

$$\tag{5.4}$$

With u and v the zonal and meridional velocities ($m.s^{-1}$), h the water depth (m), η water height variation of the free surface (m), g' the reduce gravity ($m.s^{-2}$) defined as $g' = g\frac{\rho_2 - \rho_1}{\rho_2}$ with $g = 9.81$ m.s^{-2} the gravity and the cinematic viscosity parameter $\nu = 50$ m^{2}s^{-1}.
The projection of the Navier-Stockes equation along the vertical coordinates, assuming $w \simeq 0$, can be approximate by the hydrostatic equilibrium, i.e. $\frac{\partial P}{\partial z} = -\rho g$.

5.2 Diffusive terms

Diffusive terms have been added. In the reality the cinematic viscosity coefficient of sea water is of magnitude of 10^{-6} m^2.s^{-1}, and the diffusivity acts on the dynamics at scales close to the centimeter or smaller. Here, the resolution used is of $2,000$ m. As the size of the grid is totally different from the diffusivity scale, I need to take a cinematic viscosity coefficient, higher than the observed one. I have taken the minimal limit for this grid resolution $\nu = 50$ m^2.s^{-1}. The mass diffusive term κ is taken equal to ν in order to be consistent.
With the diffusive terms, the equation becomes

$$\frac{\partial u}{\partial t} + u\frac{\partial u}{\partial x} + v\frac{\partial u}{\partial y} - fv = -g'\frac{\partial \eta}{\partial x} + \nu(\frac{\partial^2 u}{\partial x^2} + \frac{\partial^2 u}{\partial y^2}) \tag{5.5}$$

$$\frac{\partial v}{\partial t} + u\frac{\partial v}{\partial x} + v\frac{\partial v}{\partial y} + fu = -g'\frac{\partial \eta}{\partial y} + \nu(\frac{\partial^2 v}{\partial x^2} + \frac{\partial^2 v}{\partial y^2}) \tag{5.6}$$

$$\frac{\partial \eta}{\partial t} + \frac{\partial (h+\eta)u}{\partial x} + \frac{\partial (h+\eta)v}{\partial y} = \kappa(\frac{\partial^2 h}{\partial x^2} + \frac{\partial^2 h}{\partial y^2}) \tag{5.7}$$

$$\tag{5.8}$$

5.3 f-plane and β-plane

Different approximations of the Coriolis parameter are commonly used. Two famous ones are the f-plane and the β-plane. To leading order, f can be consider as constant, it is called the f-plane approximation. To second order, f is supposed to vary linearly with latitude and is approximated by $f \simeq f_0 + \beta y$, it is called the β-plane. In a first time, I will consider the f-plane, and f will be approximated by $f \simeq f_0 = 2\Omega sin(\theta)$ with Ω the angular momentum of the Earth and $\theta \simeq 60°$ the mean latitude of the Reykjanes ridge.
Due to conservation of potential vorticity, see 5.6, the flow follows closely the iso-$\frac{f}{h}$ contours. The injection creates some potential vorticity anomaly, due to vortices. If those vortices move along the gradient of $\frac{f}{h}$, relative vorticity has to compensate the change of planetary potential vorticity. Therefore, a vortex has the tendency to follow iso-$\frac{f}{h}$ contours.

5.4 Boussinesq equation and reduce gravity

The model considered is a one layer shallow water model. Indeed, only the deep water masses of the ocean are considered, so my model can be considered as a two layers shallow water model, where only the deep layer is active. To be consistent with this idea, the reduce gravity model is introduced. The reduce gravity is defined as $g_r = g\frac{\delta\rho}{\rho_{bottom}}$, with $\delta\rho$, the density difference between the bottom and the surface layer. The density of the bottom is computed by using the Boussinesq equation:$\rho_{bottom} = \rho_{top}(1 - \alpha(T_{bottom} - T_{top}))$, with $\alpha \simeq 2 * 10^{-4}$ K^{-1}.

5.5 Boundary conditions

The model is controlled at the boundaries by two conditions, the impermeability and the no-slip conditions. If the boundaries are impermeable, no fluid crosses the boundary, so in a mathematical boundary that means that the normal velocity vanishes. A fluid is no-slipping if the tangential component of his velocity is zero at the boundary. So, the tangential and the normal velocities are zero at the boundaries, in other words the horizontal velocity is null at the boundaries.
The boundary conditions considered for h are $\frac{\partial\eta}{\partial x} = 0$ at the eastern and western boundaries and $\frac{\partial\eta}{\partial y} = 0$ at the northern and southern boundaries. This means that the normal component of the height's gradient is zero at the boundaries.
A vanishing normal gradient of η at the boundary avoids spurious diffusion of mass across the boundary.
A boundary condition on η is necessary as a diffusion term κ is used.

5.6 Conserved quantity in the shallow water model: Potential vorticity

In the shallow water model the potential vorticity $q = \frac{\zeta+f}{h}$ is conserved. The potential vorticity is defined as the sum of the relative vorticity $\zeta = \frac{\partial v}{\partial x} - \frac{\partial u}{\partial y}$ and the planetary vorticity f, divided by the layer thickness. The conservation of the potential vorticity is obtained from horizontal momentum and mass advective conservation. The potential vorticity is conserved if the diffusion is neglected, on my case the Lagrangian variation of the potential vorticity is equal to: $\frac{Dq}{Dt} = +\frac{\nu}{h}(\frac{\partial}{\partial y}(\frac{\partial^2 u}{\partial x^2} + \frac{\partial^2 u}{\partial y^2}) - \frac{\partial}{\partial x}(\frac{\partial^2 v}{\partial x^2} + \frac{\partial^2 v}{\partial y^2})) - \frac{\kappa}{h^2}(\frac{\partial^2 h}{\partial x^2} + \frac{\partial^2 h}{\partial y^2})$ The planetary vorticity represents the vorticity due to the earth rotation, varying with latitudes. The conservation of potential vorticity allows that if a fluid parcel moves northward, as f increases, the fluid parcel has to increase its height h or to reduce it relative vorticity. The relative vorticity represents the dynamic vorticity, at a given latitude, due to the spatial variation of velocity field. If the relative vorticity varies, the water column height has to vary in order to conserve the potential vorticity. The figure 5.2 illustrates the conservation of potential vorticity at a given latitude, the correlation between the water column height and the relative vorticity.

Lagrangian variation of potential vorticity. If one derivates the equation on u by y and the equation on v by x of horizontal momentum local conservation and subtracts one from the

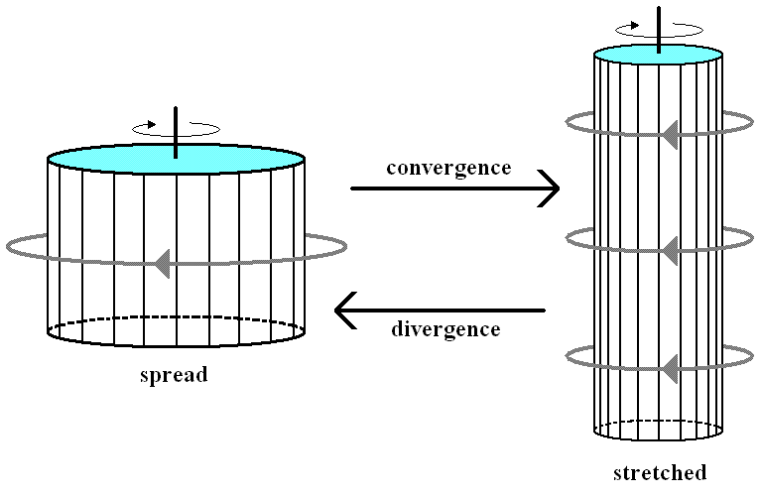

Figure 5.2: Conservation of the potential vorticity at a given latitude. If the relative vorticity varies the fluid column height has to vary to conserve the potential vorticity $\frac{D\frac{\zeta+f}{h}}{Dt} = 0$

other, one obtains:

$$\frac{\partial \frac{\partial v}{\partial x} - \frac{\partial u}{\partial y}}{\partial t} + (\frac{\partial v}{\partial x} - \frac{\partial u}{\partial y})(\frac{\partial u}{\partial x} + \frac{\partial v}{\partial y}) + u\frac{\partial \frac{\partial v}{\partial x} - \frac{\partial u}{\partial y}}{\partial x} + v\frac{\partial \frac{\partial v}{\partial x} - \frac{\partial u}{\partial y}}{\partial y} \tag{5.9}$$

$$+ f(\frac{\partial u}{\partial x} + \frac{\partial v}{\partial y}) + \cancel{\frac{\partial f}{\partial x}u} + \frac{\partial f}{\partial y}v + \cancel{g'\frac{\partial^2 h}{\partial x \partial y}} - \cancel{g'\frac{\partial^2 h}{\partial y \partial x}} = \tag{5.10}$$

$$\nu\frac{\partial}{\partial y}(\frac{\partial^2 u}{\partial x^2} + \frac{\partial^2 u}{\partial y^2}) + \nu\frac{\partial}{\partial x}(\frac{\partial^2 v}{\partial x^2} + \frac{\partial^2 v}{\partial y^2}) \tag{5.11}$$

Let's consider the case of a β-plane, with the north along the y axis, which implies $\frac{\partial f}{\partial x} = 0$, in the f-plane $\frac{\partial f}{\partial y}$ is also null.

The equation becomes:

$$\frac{\partial \frac{\partial v}{\partial x} - \frac{\partial u}{\partial y}}{\partial t} + (\frac{\partial v}{\partial x} - \frac{\partial u}{\partial y})(\frac{\partial u}{\partial x} + \frac{\partial v}{\partial y}) + u\frac{\partial}{\partial x}(\frac{\partial v}{\partial x} - \frac{\partial u}{\partial y}) + v\frac{\partial}{\partial y}(\frac{\partial v}{\partial x} - \frac{\partial u}{\partial y}) + \frac{\partial f}{\partial y}v + + f(\frac{\partial u}{\partial x} + \frac{\partial v}{\partial y}) = 0 \tag{5.12}$$

$$\iff \frac{\partial \zeta}{\partial t} + (\zeta + f)(\frac{\partial u}{\partial x} + \frac{\partial v}{\partial y}) + u\frac{\partial \zeta}{\partial x} + v\frac{\partial \zeta}{\partial y} + \frac{\partial f}{\partial y}v = \tag{5.13}$$

$$\nu(\frac{\partial}{\partial y}(\frac{\partial^2 u}{\partial x^2} + \frac{\partial^2 u}{\partial y^2}) + \frac{\partial}{\partial y}(\frac{\partial^2 v}{\partial x^2} + \frac{\partial^2 v}{\partial y^2})) \tag{5.14}$$

As f is constant on t and x, this equation can be written as:

$$\frac{D\zeta + f}{Dt} + (\zeta + f)(\frac{\partial u}{\partial x} + \frac{\partial v}{\partial y}) = \tag{5.15}$$

$$\nu(\frac{\partial}{\partial y}(\frac{\partial^2 u}{x^2} + \frac{\partial^2 u}{y^2}) + \frac{\partial}{\partial y}(\frac{\partial^2 v}{\partial x^2} + \frac{\partial^2 v}{\partial y^2})) \tag{5.16}$$

On the other hand, the mass local conservation gives:

$$\frac{\partial h}{\partial t} + \frac{\partial hu}{\partial x} + \frac{\partial hv}{\partial y} = \kappa(\frac{\partial^2 h}{\partial x^2} + \frac{\partial^2 h}{\partial y^2}) \tag{5.17}$$

$$\iff \frac{\partial h}{\partial t} + u\frac{\partial h}{\partial x} + v\frac{\partial h}{\partial y} + h(\frac{\partial u}{\partial x} + \frac{\partial v}{\partial y}) = \kappa(\frac{\partial^2 h}{\partial x^2} + \frac{\partial^2 h}{\partial y^2}) \tag{5.18}$$

$$\iff \frac{Dh}{Dt} + h(\frac{\partial u}{\partial x} + \frac{\partial v}{\partial y}) = \kappa(\frac{\partial^2 h}{\partial x^2} + \frac{\partial^2 h}{\partial y^2}) \tag{5.19}$$

$$\tag{5.20}$$

By using those two equations, one obtains:

$$\begin{cases} \frac{Dh}{Dt} = -h(\frac{\partial u}{\partial x} + \frac{\partial v}{\partial y}) + \kappa(\frac{\partial^2 h}{\partial x^2} + \frac{\partial^2 h}{\partial y^2}) \\ \frac{D\zeta+f}{Dt} + (\zeta+f)(\frac{\partial u}{\partial x} + \frac{\partial v}{\partial y}) = \nu(\frac{\partial}{\partial y}(\frac{\partial^2 u}{\partial x^2} + \frac{\partial^2 u}{\partial y^2}) + \frac{\partial}{\partial x}(\frac{\partial^2 v}{\partial x^2} + \frac{\partial^2 v}{\partial y^2})) \end{cases} \tag{5.21}$$

$$\iff \frac{1}{h}\frac{D\zeta+f}{Dt} - \frac{\zeta+f}{h^2}\frac{Dh}{Dt} = \frac{\nu}{h}(\frac{\partial}{\partial y}(\frac{\partial^2 u}{\partial x^2} + \frac{\partial^2 u}{\partial y^2}) - \frac{\partial}{\partial x}(\frac{\partial^2 v}{\partial x^2} + \frac{\partial^2 v}{\partial y^2})) - \frac{\kappa}{h^2}(\frac{\partial^2 h}{\partial x^2} + \frac{\partial^2 h}{\partial y^2}) \tag{5.22}$$

$$\iff \frac{D\frac{\zeta+f}{h}}{Dt} = \frac{\nu}{h}(\frac{\partial}{\partial y}(\frac{\partial^2 u}{\partial x^2} + \frac{\partial^2 u}{\partial y^2}) - \frac{\partial}{\partial x}(\frac{\partial^2 v}{\partial x^2} + \frac{\partial^2 v}{\partial y^2})) - \frac{\kappa}{h^2}(\frac{\partial^2 h}{\partial x^2} + \frac{\partial^2 h}{\partial y^2}) \tag{5.23}$$

$$\iff \frac{Dq}{Dt} = \frac{\nu}{h}(\frac{\partial}{\partial y}(\frac{\partial^2 u}{x^2} + \frac{\partial^2 u}{\partial y^2}) - \frac{\partial}{\partial x}(\frac{\partial^2 v}{\partial x^2} + \frac{\partial^2 v}{\partial y^2})) - \frac{\kappa}{h^2}(\frac{\partial^2 h}{\partial x^2} + \frac{\partial^2 h}{\partial y^2}) \tag{5.24}$$

□

The Lagrangian variation of the potential vorticity is depending on the diffusion terms.

5.7 Topography

5.7.1 Reykjanes Ridge

The Reykjanes ridge is represented by a Gaussian slope. The ridge starts in the middle of the domain (in y), and increases to reach $\frac{3}{4}$ho (with ho=1000 m, the sea surface height at rest without topography variation) where the ridge intersect the basin boundary. In x direction, the ridge is modeled as a Gaussian. The ridge is modeled by $ridge(x,y) = (\frac{2}{Ly} * y - 1) * ho * \frac{3}{4})e^{(\frac{(x-\frac{Lx}{2})^2)}{2\sigma^2}}$, with x the coordinate along the larger size of the basin, y the coordinate along the smaller size of the basin and Lx, Ly the domain's sizes. Figure 5.3 represents the topography used to model the Reykjanes ridge.

5.7.2 Continental shelf

In order to obtain a flow arriving perpendicularly to the ridge, I have implemented an addition a continental shelf, with a decreasing exponential all along the larger rectangular side. In the injection and upwelling areas two other topographic exponential slopes are added. This topography allows bending the iso-$\frac{f}{h}$ contours, so that contours follow the boundary. The equation of the continental slope is, with x and y the two coordinates oriented along the rectangular domain sides, Lx and Ly the rectangular domain sizes and L_{cs} the characteristic value of the exponential decreasing, $continentalshelf(x,y) = 400(exp(-\frac{Ly-y}{L_{cs}}) + exp(-\frac{Lx-x+Ly-y}{L_{cs}}) + exp(-\frac{x+Ly-y}{L_{cs}})$. Figure 5.4 presents the added topography, which correspond the continental shelf on a exponential slope all along the larger part of the rectangular basin and two other exponential slopes on the injection and upwelling corners.

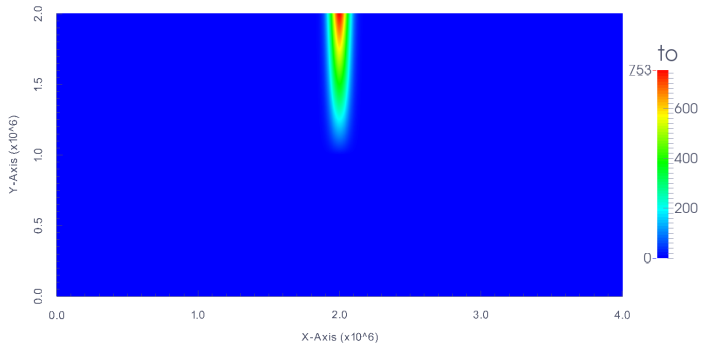

Figure 5.3: Topography of the Reykjanes ridge model.

Moreover, in the reality the Greenland-Scotland ridge is close to be as my continental shelf.

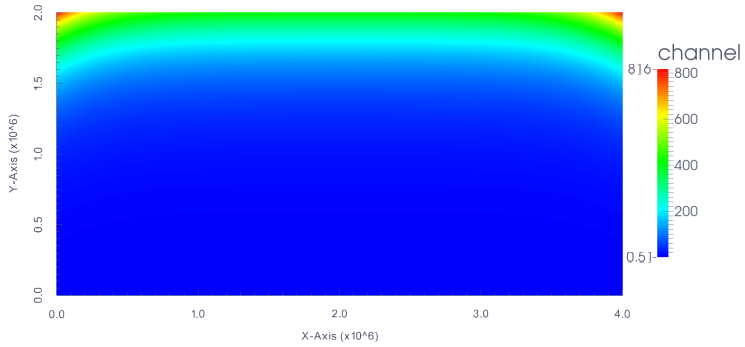

Figure 5.4: Topography added to concentrate the flow on the basin boundary. It is composed by a invariant exponential slope, and two other exponential slopes on two corners.

5.8 Injection and the upwelling

The Iceland-Scotland Overflow Water (ISOW) coming from Norwegian sea, arrives in the Iceland basin by different places but mainly by the Faroe-Shetland channel. In this basin the ISOW follows the Greenland-Scotland ridge until the Reykjanes ridge, it gets around it and continues along the Greenland-Scotland ridge.
To create the current which is going westward and crossing the ridge, water has been injected on the north-east side (i.e. the top right corner of the rectangular basin) and extracted on the north side (i.e. the top left corer of the rectangular basin). The amplitude of injection and upwelling have a profile corresponding to a quarter of a Gaussian. Those bumps are added to the shallow water equations, in the way that the water height will increase in the injection place and decrease in the upwelling place. $\frac{\partial h}{\partial t} + \frac{\partial hu}{\partial x} + \frac{\partial hv}{\partial y} = f_{inj} - f_{upw} + \kappa(\frac{\partial^2 h}{x^2} + \frac{\partial^2 h}{y^2})$.
Four different injection and upwelling strength have been used: 1 Sv, 5 Sv, 10 Sv and 15 Sv (1 Sv $= 10^6$ m^2.s^{-1}). The amount injected is always the amount taken out.
The water is injected on a 30 km section and withdrawn on a 240 km section, this difference is to avoid that the layer thickness vanishes in the upwelling region and that the model blows

up. Moreover, during the initial phase injection and upwelling are increasing from 0 Sv to the wanted amount in 50 days, to avoid an initial shock and blow up of the model
Figure 5.5 presents the injection and the upwelling bumps

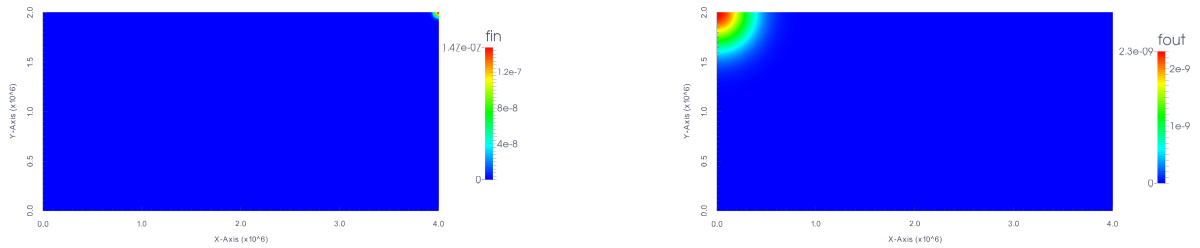

(a) Injection bump.

(b) Upwelling bump.

Figure 5.5: Those two figures represent the injection and the upwelling function. The injection, figure on the left, is a quarter of Gaussian in the top right corner of the rectangular basin. The upwelling, in the top left corner of the rectangular basin, is also a quarter of Gaussian higher standard deviation.

5.9 Age tracers

Age tracers are useful to see the temporal evolution of fluid parcels originating from a "source". Some well known tracers are ^{14}C, CFC or tritium for instance. It is a passive scalar carried by the flow, diffused and its value increases by 1 s every second, everywhere except in the source region where it is fixed to zero. The age tracers value gives the time that has passed since the water parcel left the source region.
The equation controlling the movement of age tracer is: $\frac{\partial \theta}{\partial t} + u * \frac{\partial \theta}{\partial x} + v * \frac{\partial \theta}{\partial y} = \kappa(\frac{\partial^2 \theta}{x^2} + \frac{\partial^2 \theta}{y^2}) + 1$.
Three different terms are present in this equation the Lagrangian derivative $\frac{\partial \theta}{\partial t} + u * \frac{\partial \theta}{\partial x} + v * \frac{\partial \theta}{\partial y}$, the diffusive term $\kappa(\frac{\partial^2 \theta}{x^2} + \frac{\partial^2 \theta}{y^2})$ and the age evolution +1, that mean that rest waters are older of 1 second each second.
Age tracers are also computed with a second order Runge Kutta for consistency.

Chapter 6

Numerical model

6.1 Model construction

The numerical model has been build from scratch.

6.1.1 Runge Kutta method

The mathematical model presents equations for the time evolution of the three 2D fields and their boundary conditions, u, v and h. The numerical model has to transform the continuous variables to discrete ones. To approximate the time evolution of the variables, I have implemented a second order Runge Kutta system. The Runge Kutta method is a numerical analysis used to approximate solutions of ordinary differential equations $\dot{y} = f(y,t), y(t_0) = y_0$. In order to compute the temporal derivative, this method computes the derivative at the time step $\delta t/2$,and uses this value to compute the value at the time step δt, by using this formula: $y_{n+1} = y_n + \delta t f\left(t + \frac{\delta t}{2}, y_n + \frac{\delta t}{2} f\left(t, y_n\right)\right)$. This method is more precise than the Euler method, this method is an order two method so the error is of the order of δt^3. Of course, the result can be more precise if one uses a order four Runge Kutta method, but the computing time becomes longer. The implementation of the order two Runge Kutta method is done like that:

$$y_{n+\frac{1}{2}} = y_n + \frac{\delta t}{2} f\left(t, y_n\right) \tag{6.1}$$

$$y'_{n+\frac{1}{2}} = f\left(t + \frac{\delta t}{2}, y_{n+\frac{1}{2}}\right) \tag{6.2}$$

$$y_{n+1} = y_n + \delta t y'_{n+\frac{1}{2}}. \tag{6.3}$$

The spatial derivative are computed with a centered limit difference approximation.
In order to improve the precision all the computations are done with double precision.

6.1.2 Boundary conditions

The boundary in the model has to represent the boundary in the reality, to a certain point of course, the boundary will be simplified, the boundary conditions considered are no-slip conditions. The no-slip conditions impose no tangential and normal velocities at the boundary, i.e. $u = 0$ and $v = 0$ at the boundary. Those conditions create a reduction of the speed near the boundary due to the viscosity. Coastal Kelvin waves are observed when the Coriolis force is taking into account. One can see the Coastal Kelvin waves on figure 6.1.
And, the second boundary condition is that the normal variation of the surface height is forced to vanish at the boundary.

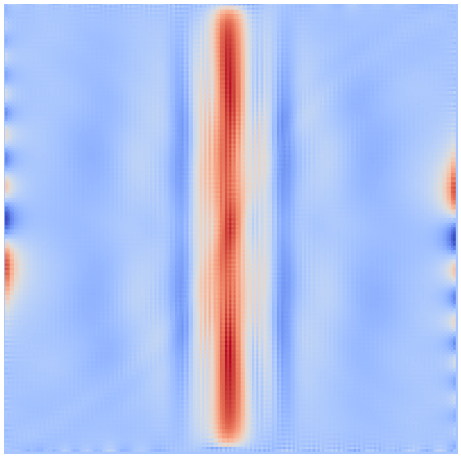

Figure 6.1: Sea surface elevation of the basin after a computation of four days with a crest along x as initial condition, with a grid of $202 * 202$ points in a rotating frame. The major part of the crest is still at the center, and on both sides the propagation of coastal Kelvin waves.

To implement those conditions, at the edge of the grid velocities. However, as the model is implemented with a centered derivative method and that the diffusion terms are considers (second order), I need a value just on the other side of the gird for the computation of the edge of the grid. So, my computational grid is surrounded by a value of null velocities and the symmetrical value of η across the grid to prevent diffusion of layers thickness. Compare with the edge of this computational grid, i.e. the implemented grid is bigger than the computational grid.

6.1.3 Arakawa grids

The model can be implemented with different grid patterns, they are called Arakawa grids. The two components of the velocity and the surface height can be considered at different positions of a grid, as one can see on figure 6.2. The A grid is implemented with the velocities and the surface height at the same position. The B grid is implemented with the velocities on a grid and the surface height on a different one, with the points of one grid on the middle of the other grid. The C grid corresponds to the surface height at the vertices of the gird and the velocities, respectively on the x and y axis for u and v. In this grid, the velocities are between two surface heights. In each case, there are pros and cons, in the B and C cases a mean over the vicinity points has to be effected to compute the shallow water equations. The A gird is the only grid which is un-staggered.

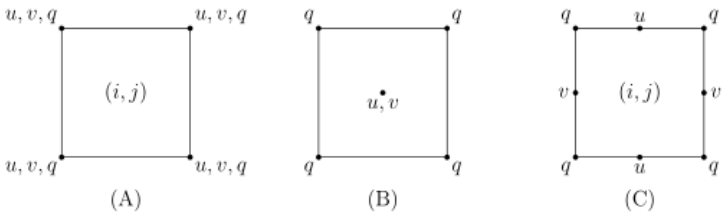

Figure 6.2: Different Arakawa grids.

In this study, the A grid has been used, because it is the simple to implement (avoid means) and there is in my cases no good reason to use an other one.

6.2 Conditions of numerical stability

In order to avoid numerical instability, different conditions have to be verified.
The first stability condition is the Courant-Friedrichs-Lewy condition, this condition (cf. equation (6.4)) characterized the maximum time step (dt) that one can used with a defined phase velocity $\sqrt{g'H}$ and the model's grid spacing (dx). The time step has to be smaller than the advective time scale :

$$dt < dx/(4\sqrt{g'H}) \tag{6.4}$$

The second condition is on the cinematic viscosity parameter. The viscosity allows the dissipation of energy flow at small scales, around millimeter scales and the cinematic viscosity parameter has a magnitude of $\nu = 10^{-6}$ $\mathrm{m^2 s^{-1}}$. However, my model's grid is far from the millimeter dimensions but closer 2 km. The diffusion time scale has to be higher than the model's time step in order to avoid stability problems, cf. equation (6.5). To satisfy this stability condition, with my grid's dimension, I have to take a cinematic viscosity parameter equal to $\nu = 10^2 - 10^3 \mathrm{m^2 s^{-1}}$.

$$dt < dx^2/\nu \tag{6.5}$$

6.3 Munk layer dimension

The objective of this study is to study the behavior of a boundary current, in order to visualize this current, a condition on the cinematic viscosity parameter and on the horizontal steps have to be validate. The Munk layer dimension is defined as: $\delta_m = (\nu/\beta)^{1/3}$, this dimension is the typical dimension of the boundary layer thickness. To represent this current, I want that the horizontal resolution δx is about ten times smaller.

6.4 Model validation

Now that the basic numerical stability of the model is discussed, I have to control that the model is a correct rotating shallow water model and that the boundary conditions are correctly implemented. This part is capital because a small mistake can be hidden in the code and change everything under some conditions, so I have to vary most of the parameters and validate that the model is always consistent with the analytical results.
For the model validation, the domain is less precise than the one adopted for computation, and the grid is taken square.
For elementary initial conditions, velocity and water height evolutions are well known. Thanks to that, different initial conditions have been applied to the model, a Gaussian crest along x but constant in y, an other one along y and constant in x, two other ones along each diagonal, a circular elevation of the height placed in the middle on the grid and to finish different dipole combinations. The size of the horizontal steps and the value of the cinematic viscosity coefficient have also been changed to different values. Figures 6.3 present the different initial conditions used for the model validation.

6.4.1 Divergence and potential vorticity

Divergence and potential vorticity are very useful to analyze the system. The divergence allows seeing the fast phenomenon, as Poincare waves. Indeed, the divergence represents velocity's variation along an axis relatively to this axis. Wave's propagation are, with this tool, easy to

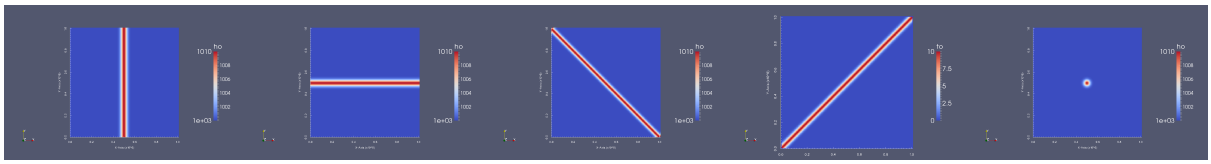

(a) Crest along x (b) Crest along y (c) Anti diagonal crest (d) Diagonal crest (e) Circular elevation

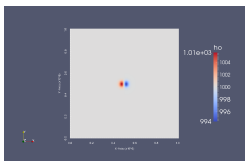

(f) Southward dipole

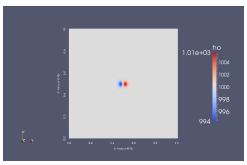

(g) Northward dipole

Figure 6.3: Different initial sea surface height, that hto follow a negative gradient of potential vorticity, vortices have to ave been used to test the consistency of the model.

identify. On the other hand, the potential vorticity is very useful to analyze slow phenomenon, like oceanic or meteorological phenomenons.

6.4.2 Phase velocity

The phase velocity is defined by $\sqrt{g_r h}$, with $g_r = 9.81 * 10^{-3}$ m.s^{-2} to follow a negative gradient of potential vorticity, vortices have to the reduce gravity and $h = 10^3$ m the surface height, so $C_{phase}^{theo} = 3.13$ m.s^{-1}. The time to a return obtained with the simulations is $T_{return}^{simul} \simeq 324000$ s $= 3$ days $+ 18$ h, so the phase velocity obtained with the simulations is $C_{phase}^{simul} = \frac{Lx}{T_{return}^{simul}} \simeq 3.09$ m.s^{-1}. The two phase velocities are close, the small difference between the expected and the obtained one can be explain by the precision on the time to a return and maybe the variation of h on the theoretical computation. This test is not validating my model but only showing that it is not inconsistent on this point.
Then, the zonal velocity has to verified $u = C_{phase} \frac{\eta}{H}$, with H the mean surface height and η the surface perturbation. The computation gives $u \simeq 10^{-2}$ m.s^{-1} and the simulations shows values varying around this value.

6.4.3 Crest along x

I consider a crest along x as the initial conditions. In the absence of the Coriolis force, a crest propagates in both directions, with the wave speed $\sqrt{gh}$ (if the crest is a Gaussian in x, i.e $\eta(x) = \eta_0 e^{-x^2}$, the propagation will be in the x direction). When the crest encounters the boundary, it will be reflected. The presence of the viscous terms implies that the propagation close to the side is slower than in the middle of the grid.
Of course those analysis have been applied to the crest along y and diagonal crests, the results will not be presented here because they are the sames than for the crest along x. However, they are not less important, they allow to validate that the model reacts in a good way in all directions. The Coriolis force is not consider to just validate that the pressure gradient force, the advection, the diffusion and the temporal variation are well implemented. On a second time the Coriolis force will be added, the Coriolis force's influence and the geostrophic equilibrium will be observed.
In the presence of the Coriolis force, a part of the crest is emitted as Poincare waves (divergence part), and an other one (potential vorticity part) verifies the geostrophic equilibrium and stays

at the same position.

6.4.4 Circular elevation

On the other hand, circular elevations have been implemented as initial conditions of the sea surface height. In the absence of the Coriolis force the elevation propagates and reflects at the boundaries as if this elevation was due to the impact of a stone in a pond. But in the presence of the Coriolis force, thanks to the geostrophic equilibrium, this elevation induces a vortex, cyclonic for a negative elevation and anti-cyclonic for a positive one. This vortex stay at this initial position, a Poincare wave is emitted in a first time, but the major part of the energy stay with the vortex.

6.4.5 Cinematic viscosity parameter

On the one hand, the cinematic viscosity parameter has been changed, varying from 10^-1 to 10^5 $m^2.s^{-1}$. The higher the cinematic viscosity parameter, the slower the crest propagates. The cinematic viscosity parameter has to verified the relation between the time step δt and the viscosity time scale $\delta x^2/\nu$.
As said before, if the cinematic viscosity parameter is to small, the model can blow up. The cinematic parameter is taken as small as possible to be as close as possible from the reality but nor to small to not blows up.

6.4.6 Error convergence

The theoretical mean of the surface elevation, for a crest along x as a condition initial, is $\eta_{mean} = \frac{\mathcal{A}_{gaussian}}{nx} \simeq 0.5$ m. The simulation mean is varying around 0.5 m with values between 0.45 m and 0.55 m, this variation can be explain by the fact that my model is not continuous but discrete and in this case the mean is effected not in the real function but only in the points of the grid.
The number of horizontal steps nx, ny have been changed, three values have been tested: 100, 200 and 800. Of course, the larger nx, the better the resolution, but the longer the compilation. When the number of horizontal steps $\delta x, \delta y$ is larger, the resolution $dx = L_x/nx, dy = L - y/dy$ is better and the phenomenon can be observed in a better way, if the resolution is too small, some currents can be less represented, for example in some oceanic models the Gulf Stream is represented by only one point in the zonal axis, in those cases the Gulf Stream can not be studied in a good way. And the variation of the number of horizontal steps allows to be the behavior of the models with different resolutions.
In order to conserve the same value $\frac{dx}{4\sqrt{g'Hdt}}$ uses for the Courant Friedrichs Lewy condition, when dx is divided by two, dt is also divided by two.
When the resolution has been increased, the error has diminished. This study could have been improved by first, for a specific dt varying only dx, and after for a specific dx varying only dt. But, that should have take us to many time, and that is not aim of this study.

6.4.7 Dipole validation

Dipole configuration is also useful to cheek the implementation, when the two poles of the dipole are close and strong enough, they are influencing each other and will move. For example, in the case on a negative elevation (cyclonic) on the east and a positive one (anticyclonic) on the west, the dipole will go southward.The dipole simulation is very interesting, as one can see on this one

the two characteristics of the system, the divergence which represents the wave's propagation and the potential vorticity which represents the vortex movements.

6.5 Topography

Whereas in reality the ridge goes out water at the Iceland place, my model ridge is everywhere under water to avoid the vanishing of the surface layer leading to numerical problems. Indeed when the water height vanishes and becomes negative, the model blows up.

6.6 Programming language

For this study the fortran 90 programming language has been used. The compilation has been done principally with the Intel(R) Fortran Compiler. The uses of gfortran has been effected during the validating part, indeed the debugging tools of both compilers have been used, to once again validates that the code was well implemented. The runs have been submitted to and run on in "batch" mode the calculators of the LEGI laboratory. The data has been created in netcdf format, and visualized thanks to the software Paraview.

Chapter 7

Results

Experience number	ν ($m^2.s^{-1}$)	Injection (Sv=10^6 $m^2.s^-1$)	Reduce gravity ($m.s^-2$)	Reynolds number
1.1	50	1	1.96×10^{-2}	20
1.5	50	5	1.96×10^{-2}	100
1.10	50	10	1.96×10^{-2}	200
1.15	50	15	1.96×10^{-2}	300
2.1	50	1	9.81×10^{-3}	20
2.5	50	5	9.81×10^{-3}	100
2.10	50	10	9.81×10^{-3}	200
2.15	50	15	9.81×10^{-3}	300

Table 7.1: *table of experiments*

7.1 Qualitativ analysis

This part presents the behavior of the flow for different ocean currents: experiments 1.1, 1.5, 1.10, 1.15. At the end, we also mention result from runs with a lower Rossby radius of deformation, closer to observed values in the region around the Reykjanes ridge, see 7.2.6.
All the simulations are continued for 1200 days at least (experiment 1.1 and 2.1) and up to 2100 days (experiments 1.15 and 2.15) to obtain a stationary state for the circulation around the ridge.

7.1.1 β-plume and iso-$\frac{f}{h}$ contours

A β-plume is a plume evolving along a line of iso planetary vorticity, (iso-$\frac{f}{h}$), in a westward direction.
The iso-$\frac{f}{h}$ contours are important because they are the preferential way to move for the flow. Indeed, a flow with a given vorticity will follow a given iso-$\frac{f}{h}$ to conserve his potential vorticity. The iso-$\frac{f}{h}$ contours are influenced by three main terms: the β-effect that changes the value of f with latitudes, the ridge topography that turn the contours around the ridge and the continental shelf topography moving the contours parallel to the basin boundary close to the continental shelf.
The flow, in our model, has the tendency to follow the iso-$\frac{f}{h}$, it is evolving laminarly for the lowest injection and like a β-plume for the higher injection values.

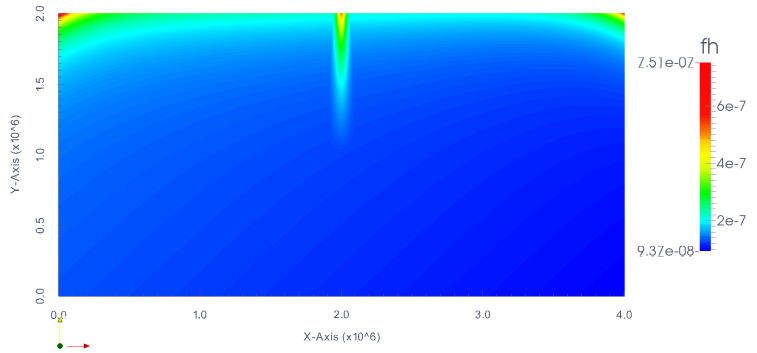

Figure 7.1: Iso-$\frac{f}{h}$ contours. Three areas can be distinguished. The part in the bottom of the rectangle, where the contours are mainly given by the β-effect, with iso-$\frac{f}{h}$ contours perpendicular to the north-south axis. The second part is the ridge area, the contours follow mainly the topography of the ridge. And the third one, at the top of the rectangle, which is dominating by the continental shelf topography, iso-$\frac{f}{h}$ contours follow the basin boundary.

7.1.2 1 Sv injection

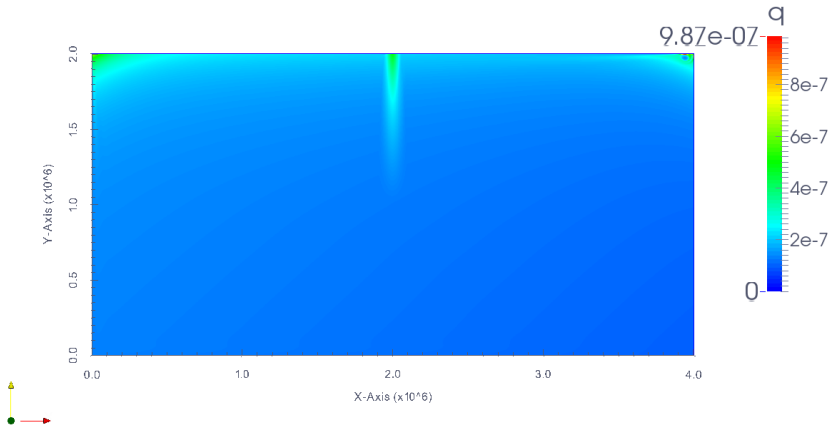

Figure 7.2: Potential vorticity for the 1 Sv injection, i.e. experiment 1.1, after 1200 days. The flow follows the iso-$\frac{f}{h}$ contours, from the injection to the upwelling area.

In this, the injection and the upwelling are quite low, i.e. 1 Sv. The flow injected in the north-east corner follows the edge of the domain up to the ridge. The flow is near the northern boundary because of the β-plane and the continental shelf. Indeed, as explain in 5.3, the flow has tendency to flow along isolines of $\frac{f}{h}$. In my case the north is not on the top of my domain but the north-south axis is tilted by $+45°$. In the case without the continental shelf topography the flow is not following the edge of the domain but goes westward. The continental shelf allows the flow to follow the edge and to arrive at the Reykjanes ridge as in reality, i.e. following the Greenland-Scotland ridge.

When the flow encounters the ridge a small part crosses directly over the ridge but the major part continues along the ridge up to the tip before it crosses. The dynamics is governed by the iso-$\frac{f}{h}$ contours. At the tip of the ridge (the farthest part from the basin boundary), the flow stops going south-westward, turns around the ridge and continues along the northern part of the ridge. The amount that crosses the ridge before the end of it goes also back following the ridge along lines of constant $\frac{f}{h}$.
After that the flow goes northwestward to the upwelling region where it is withdrawn. A small asymmetry with respect to the ridge is observed due to the asymmetry of the iso-$\frac{f}{h}$ contours, the β-plume and inertial overshoot.
So, for a small water injection the behavior is quite simple, the flow mostly follows the iso-$\frac{f}{h}$ contours, i.e. follows the edge, the Reykjanes ridge and the edge again, from the injection to the upwelling places.

7.1.3 5 Sv injection

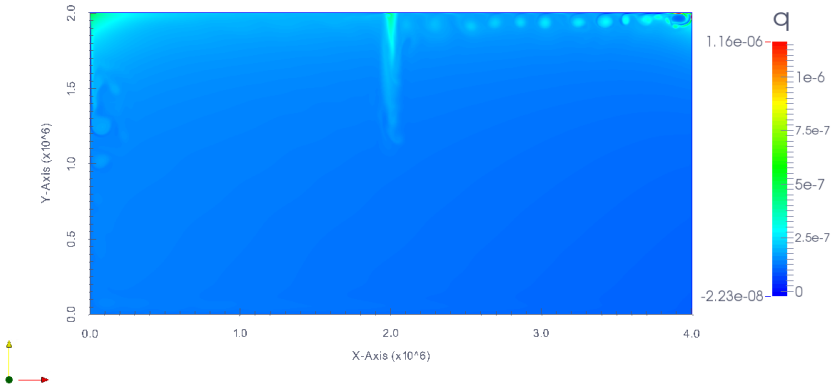

Figure 7.3: Potential vorticity for the 5 Sv injection, experiment 1.5, after 1200 days. From the injection to the ridge, the flow organizes into small vortices. All along the ridge, the enstrophy is high. An asymmetry is present between the two parts of the ridge, particularly at the area where the flow turns around the ridge. And from the ridge to the upwelling region, a continuous flow is present.

In this case, 5 Sv of water is injected. The flow injected is formed by small vortices propagating form the injection to the ridge. The trajectory of the flow is quite similar to that of the 1 Sv flow. Those small vortices vanish while they cross the ridge and the flow is continuous on the northern part of the ridge. Figure 7.3 shows the different structures of the flow: the small vortices before the ridge, the flow turning around the ridge and next the continuous flow to the upwelling region.

7.1.4 10 Sv injection

With an injection of 10 Sv, experiment 1.10, the motion is qualitatively different. The flow arrives on the ridge as a succession of coherent vortices. Let's have a look at the motion and

behavior of a vortex while it crosses the ridge. When the vortex arrives at the ridge following the basin boundary, it follows the south-eastern part of the ridge. During this motion the vortex stretches, the part closer to the tip of the ridge continues along the ridge, while the other part crosses the ridge and follows the ridge to his north-eastern part. A long filament between the two parts, is created all along the ridge. This filament breaks. The part closer to the basin boundary evolves in waves propagating along the basin boundary. The other part, i.e. the part closer to the tip of the ridge, evolves in a vortex going northward separating from the ridge.

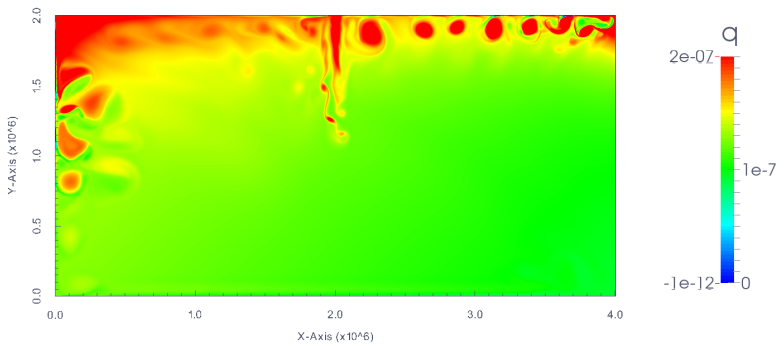

Figure 7.4: Potential vorticity for the 10 Sv injection, experiment 1.10, after 1200 days. From the injection to the ridge, the flow is formed by vortices. All along the ridge, the vorticity is high. Asymmetry is present between the two parts of the ridge, particularly at the area where the flow turn around the ridge. Some eddies propagates along the basin boundary and episodically some of them split off from the ridge.

So, when the flow of vortices crosses the ridge, it is converted to two different phenomena: small vortices and waves who propagate northward.

7.1.5 15 Sv injection

The maximum injected flow is 15 Sv, experiment 1.15. With this injection, big vortices are created in the flow. The motion of one of those vortex is the following:
The vortex arrives to the higher part of the ridge, at this point the vortex is compressed onto the ridge. Above the ridge, the potential vorticity is high, a piece of low potential vorticity (negative vorticity) is locked between those the high potential vorticity above the ridge and the vortex high potential vorticity. The vortex further stretches while moving along the ridge, south-westward. The core of the vortex is leading the displacement. The tail of the vortex crosses the ridge and stretches out, due to the shear above the ridge, to form a filament. The vortex shrinks, leaving potential vorticity to the filament. When the vortex arrives close to the end of the ridge, the core of the vortex winds up again and moves northward separating from the ridge. In the area north of the ridge, we observe a chaotic interaction of eddies and filaments. Each eddy arriving at the ridge is disintegrated into several eddies at the ridge which then proceed towards the upwelling area.
So, the ridge converts strong coherent vortices into a larger number of smaller vortices and filamentss, interacting chaotically.

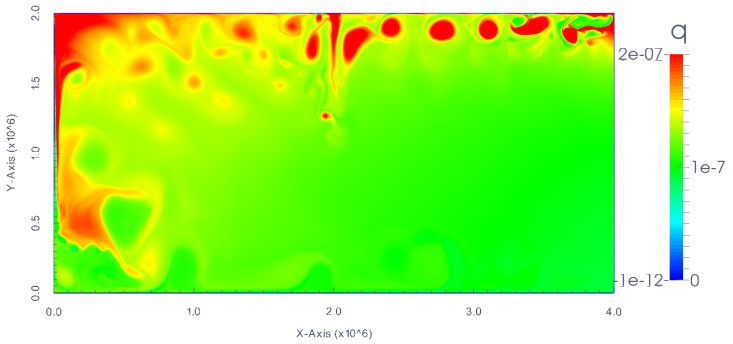

Figure 7.5: Potential vorticity for the 15 Sv injection, experiment 1.15, after 1200 days. From the injection to the ridge, the flow is formed by big vortices. All along the ridge, the vorticity is high. The asymmetry is conspicuous between the two parts of the ridge. A part of the flow continue along the ridge and the basin boundary with eddies structures. An other part of the flow, forms eddies and splits off form the ridge.

7.2 Quantitative analysis

7.2.1 Reynolds number

The Reynolds number represents the ratio of inertial terms in front of viscous terms. *Edwards and Pedlosky* [1998] compute it using the volume transport: $R_e = \frac{Q}{h_0 \nu}$, with Q the volume transport, $h_0 = 1,000$ m the water height at rest without topography. The Reynolds numbers obtain in the numerical model is equal to $R_e = 20 \frac{Q}{1Sv}$, with $Q = 1, 5, 10, 15$ Sv.

7.2.2 Hovmoller diagram

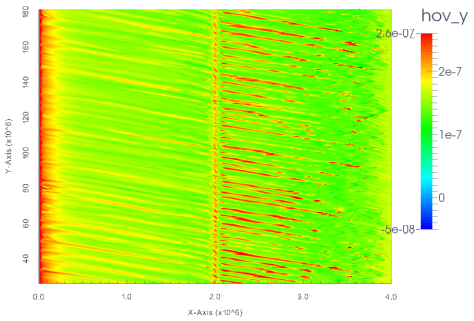

(a) At 1900 km.

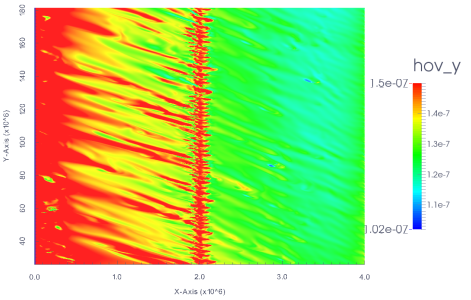

(b) At 1800 km.

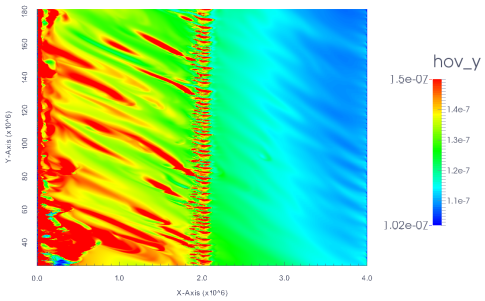

(c) At 1700 km.

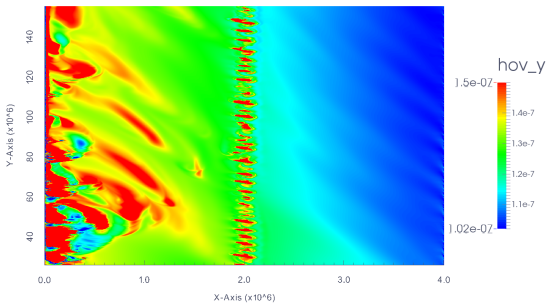

(d) At 1600 km.

Figure 7.6: Hovmoller diagram at different section parallel to the long side of rectangle, representing along the x axis. Starting 300 days after the beginning of the 15 Sv injection, during 1500 days, time along the y axis in second.

Hovmoller diagrams allow to see the propagation of waves in time. I used it to see the propagation before and after the ridge of waves and vortices.
Hovmoller diagrams have been done along a parallel section of the long side of the rectangle. Figure 7.6 presents some of them, for the injected flow of 15 Sv, experiment 1.15. The closer to the longer side of basin boundary, the faster are the waves and eddies.
For each of those sections, the waves and eddies velocities is the same before and after the ridge. Indeed those sections, are very close to follow the iso-$\frac{f}{h}$ contours.

Distance of the section from the longer bottom slide of the rectangular basin	Waves and eddies velocity (m.s$^-$1)
1900	12 cm.s^{-1}
1800	6 cm.s^{-1}
1700	4 cm.s^{-1}
1600	2 cm.s^{-1}

Table 7.2: *Waves and eddies velocity for different sections of the* 15 *Sv injected flow.*

The table 7.2 presents the waves and eddies velocities of each section of the injected flow of 15 Sv. Two different behaviors are present the fast waves going along the basin boundary and slow eddies coming from the tip of the ridge. The increase of the speed with approaching the edge is explained by an increase of the mean velocity and the topographic β effect, the continental slope increases exponentially approaching the edge.

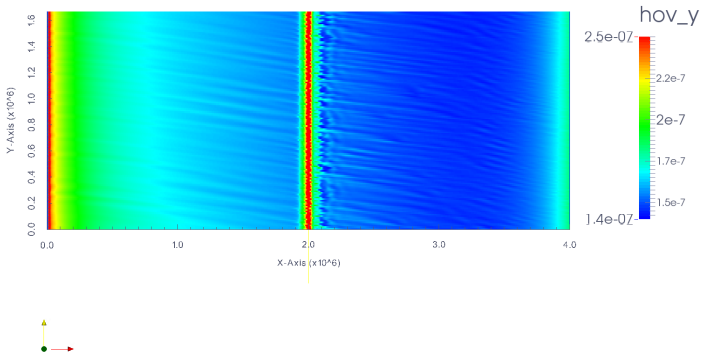

Figure 7.7: Hovmoller diagram for a section parallel to the long side of rectangle, at 1900 km from the southwestern edge, representing along the x axis. Starting 300 days after the beginning of the 5 Sv injection, experiment 1.5, during 1500 days, time along the y axis in second.

The figure 7.7 represents the Hovmoller diagram for a 5 Sv injected flow on the first section, i.e. at 1900 km from the base of the larger rectangle basin, the waves velocity is the same than for the 15 Sv injected flow.
So there are two differences due to the variation of the strength of the injected flow are strong. First, the intensity of the waves are different. And second, when the injected flow becomes strong enough some eddies detach form the tip of the ridge.

7.2.3 Scale of motion: Taylor scale

To analyse the horizontal scale of the dynamics, I use averaged kinetic energy divided by time averaged enstrophy (square of vorticity), $\lambda_1 = \sqrt{\frac{\langle u^2+v^2 \rangle}{\langle \zeta^2 \rangle}}$, it is close to the Taylor scale (with a factor $\sqrt{5}$ difference, see *Boffetta and Ecke* [2012]), and is a good characteristic of the size of the velocity gradient. In figures 7.8, we divided the Taylor scale by the Rossby radius of deformation.

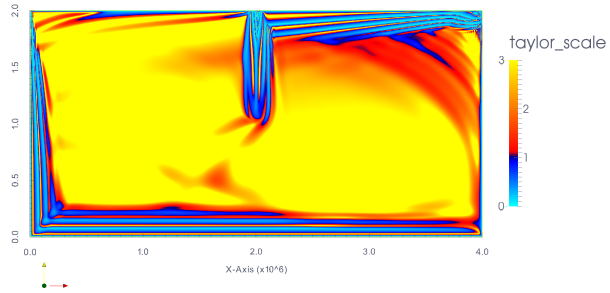

(a) Starting 300 days after the begining of the 1 Sv injection, mean on 1200 days.

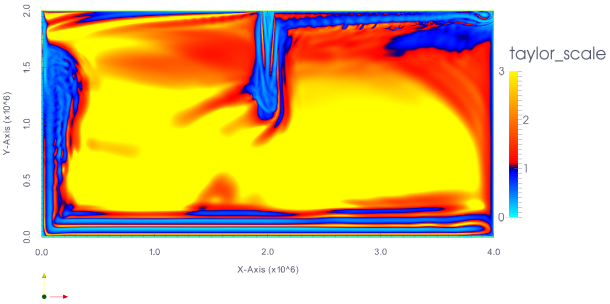

(b) Starting 300 days after the begining of the 5 Sv injection, mean on 1200 days.

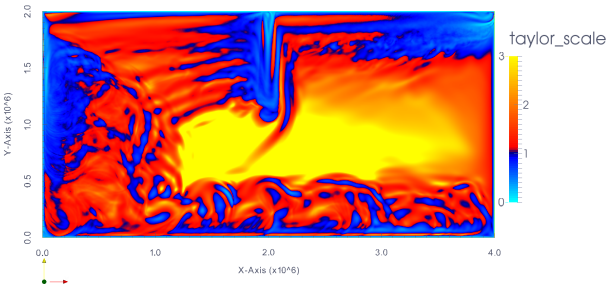

(c) Starting 300 days after the begining of the 15 Sv injection, mean on 1500 days.

Figure 7.8: Taylor scale divided by the Rossby radius of deformation, $\lambda_1 = \frac{1}{L_R}\sqrt{\frac{\langle u^2+v^2 \rangle}{\langle \zeta^2 \rangle}}$, of the circulation around the ridge. The blue parts represent places where the square of vorticity is high compare with the kinetic energy. At the contrary red and yellow parts are places where kinetic energy is predominant in front of square of vorticity.

On all figures 7.8, an asymmetry is present between both sides of the ridge. The different patterns are limited by contours which correspond to iso-$\frac{f}{h}$ contours. For the higher injection cases, some tongues of small scale detach from the ridge along the iso-$\frac{f}{h}$, like some β-plumes.
On the first figure (1 Sv, experiment 1.1), the flow is laminar, the Taylor scale is structured in different areas. On the area situated between the injection and the ridge, an alternation of higher and smaller than 1 tongues is present. The flow is laminar and stationary, those tongues are explained by bands of constant velocity of the laminar flow and the variation of the sign of the relative vorticity. Around the ridge area, the phenomenon is quite similar, the flow turning around the ridge is still laminar, the relative vorticity non null. The tongue of Taylor scale appears. For a laminar flow the Taylor scale is often not very useful as it oscillates between large values where vorticity vanishes and velocity has either sign. The signature of the banded structure, however, survives in the turbulent flow (see below), this is why it is presented here.
On the second figure (5 Sv, experiment 1.5), the flow is no longer laminar. On the part between the injection area and the ridge, the flow is a chain of eddies. The high relative vorticity is a signature of the eddies. On the ridge area, the flow turns around the ridge, an asymmetry is present in different areas. On the southern side, the flow is turning smoothly to the ridge tip, whereas on the other side the flow goes abruptly to the basin boundary. Second, after turning around the tip, the flow is, in part, deviating from the ridge and the signature of eddy streets appear and a kind of horn of small scales is present at the beginning of the street. On the part going from the ridge to the upwelling area, the flow is laminar and the Taylor scale is here not very interesting.
On the third figure (15 Sv, experiment 1.15), the flow is fully turbulent, the size of the eddies between the injection area and the ridge is higher than for other cases. Around the ridge, the asymmetry is conspicuous. The path of eddies to the tip of the ridge is well define by the red stripe. In the red stripe the velocity is high in front of the vorticity. Eddies turn around the tip of the ridge, creating a bulb in the figure of the Taylor scale. Some stripes are present on the northern part of the ridge, due to the eddies leaving the ridge. These eddies than travel along lines of constant planetary vorticity as a succession of β-plumes. The ridge represents an extended source of β-plumes.

7.2.4 Age tracers

Age tracers evolve with the same patterns than the relative vorticity. The figure 7.9, injected from the injection area after 1100 days.

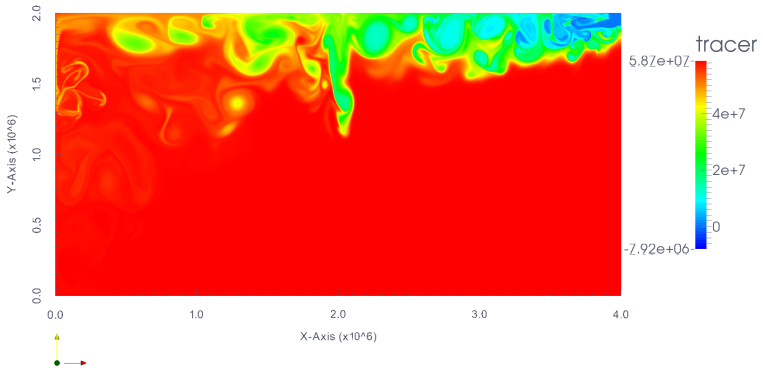

Figure 7.9: Age tracer, 1100 days after the beginning of the 15 Sv injection.

After 120 days the first injected water arrives to the ridge. And after 300days the first injected water parcels arrive to the upwelling area.

7.2.5 Flow over the ridge

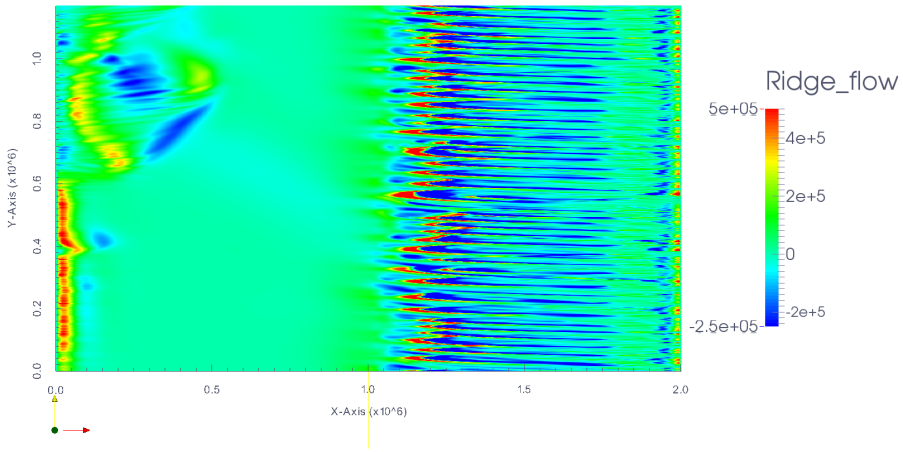

Figure 7.10: Flow over the section along the axis of the ridge, representing along the x axis and along time in days. Starting 300 days after the 15 Sv injection and during 1500 days.

The figure 7.10 represents a cross section of the transport $u(h+\eta)$ along the crest of the ridge (Hovmoller diagram). Almost periodic patterns are observed. This is, lines of positive and negative velocities representing structures evolving, with almost constant speed down the ridge followed at the tip of the ridge by a strong anomaly of a positive velocity south of a negative velocity corresponding to an eddy. The pattern moves along the ridge with an average velocity of 10 cm.s^{-1} and repeat every 40 days.

7.2.6 Low Rossby Radius length

The Rossby radius of deformation used in the experiments 1.1 to 1.15 is of 35 km. To be closer form observed values near the Reykjanes ridge, I diminish the Rossby radius of deformation by dividing the reduced gravity value by two, corresponding to a $\sqrt{2}$ division of the Rossby radius of deformation.

Chapter 8

Laboratory experiments

8.1 Optical method of altimetric imaging velocimetry

In the experiments, we used an altimetric imaging velocimetry optical method. This method allows to have a very high spatial and temporal precision on the surface elevation, the velocity and the vorticity. This method has been developed by *Afanasyev et al.* [2008] and is explained in further detail below.

8.1.1 Principle

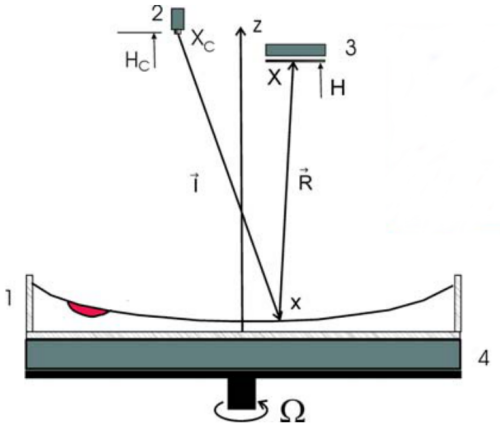

Fig. 1 Sketch of the experimental setup: rotating tank (*1*), photo/ video camera (*2*), lamp box with color slide (*3*) and a lamp box for the optical thickness measurements (*4*). *Red lens* shows schematically lighter fluid dyed with red color and injected at the surface for the optical thickness tests.

(a) Optical sketch.

(b) Color pattern.

Figure 8.1: Sketch of the optical method and Lab pattern. From *Afanasyev et al.* [2009].

The experimental setup is sketched in figure 8.1. The surface of a fluid in a rotating tank adopts a parabolic form, when in solid body rotation. By projecting an illuminated picture (considered at infinity) on the parabola formed by the solid body rotation, one can obtain, by reflexion on a single camera placed in the image focus, the reflexion of this image. The darker the room and the tank, the better the quality of the image.
In order to see any elevation of the free surface, a specific color pattern image is projected on

the fluid surface, with a linear variation of colors in x and in y directions. The color pattern used for the experiments is called Lab color space, see figure 8.1.

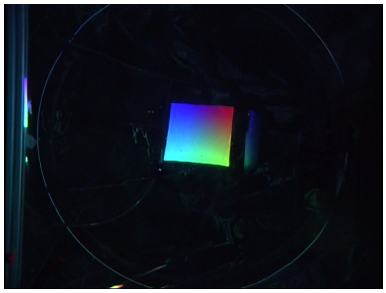

(a) Without rotation.

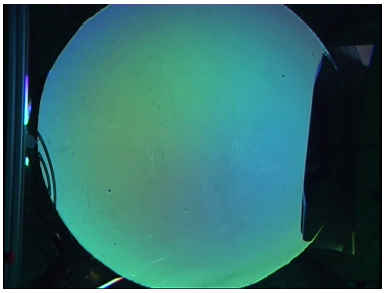

(b) With rotation.

Figure 8.2: Laboratory observations with and without rotation. Before solid body rotation, the reflected image has the size of the projected image. With solid body rotation, the reflected image cover all surface, $\Omega = 0.82$ tour.s^{-1}.

Any variation in height of the fluid surface, represents a deformation of the mirror and a shift in the projected colors. On the parabola surface, the three colors are both at 120° of each other. When a perturbation of the surface appears, the reflected colors change. Indeed, a slope of the water height oriented in a given direction is colored by a color links with the direction. By comparison with the initial color reflexion, one can detect any perturbation of the surface, with a high precision. This color variation gives a gradient of surface pressure. This gradient pressure, thanks to the geostrophic balance (or any other balance), gives the velocity field, and derived quantities such as vorticity. Since the surface height variation is optically amplified over a large distance. This method is very precise. One can obtain a velocity vector for each pixel of the image, the experiment camera resolution is $480 * 720$ pixels and $\Delta h_{min} = 1$ micron (see *Zhang and Afanasyev* [2013]).

8.1.2 experimental parameters

This method has been installed on the rotating tank, during a visit of Afanasyev to the LEGI. The rotating tank diameter is 1.30 m, the rotation speed is $\Omega = 0.42$ tour.s^{-1}. The experiments have been done with two fluids, a salty one, with a density of $1,039$ kg.m^3 and another injected with a density of $1,016$ kg.m^3.
An effort has been made o approach the nondimensional numbers, L_R, the Rossby radius of deformation and R_d, in reality and the numerics The experimental planetary vorticity is given by the tank rotation: $f = 2 * \Omega = 5.27$ rad.s^{-1}. The surface height of a parabola surface is given by the formula: $h(r) = h_0 + \frac{\Omega^2}{2*g}(r^2 - \frac{R_{tank}^2}{2})$ (see *Zhang and Afanasyev* [2013]), with R_{tank} the radius of the tank, r the radius position and h_0 the surface height without rotation. In the laboratory experiments, the ratio between the Rossby radius of deformation $L_R = \frac{\sqrt{g'h_0}}{f} = 3$ cm, (with g' the reduce gravity, computed thanks to $\rho_1 = 1,016$ kg.m^3 and $\rho_2 = 1,039$ kg.m^3, $h_0 = 0.12$ m the water height at rest without topography and $f2 * \Omega$ the Coriolis parameter) and the ridge length is around 20 cm. And $L_R = 3$ cm corresponds to vortices of about 6 cm in diameter. This ratio is consistent with the numerical simulations.

8.1.3 Difference between numerical and experiment models

The ridge has not been tilted like in the numerical model, it is oriented along the north-south axis. In the numerical simulations, a reduced gravity model has been used to model the upper

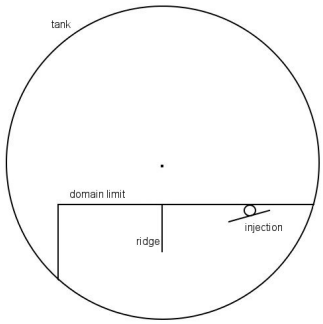

(a) Top view of the tank.

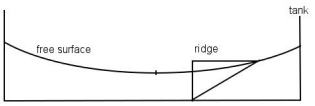

(b) Side view of the experimental setup and the ridge.

Figure 8.3: Sketches of the experience, with on the left the top view and on the right a cut along the ridge direction.

layer, whereas in the laboratory experiments the problem is inversed. Since measurements are obtained from the free surface, the model is turned upside down, i.e. the upper layer is at the bottom, and the layer that we consider is on the top and also the ridge is turned upside down. Figures 8.4 present the numerical and experimental model sketches.

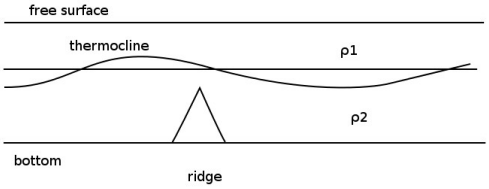

(a) Numerical sketch.

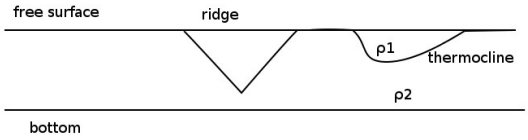

(b) Experimental sketch.

Figure 8.4: Sketches of the numerical and experimental models. The experimental model is And upside down compare to the numerical one, the base of the ridge is on the top, the bottom layer is on the top and less dense, and the upper layer is on the bottom.

8.2 Results

8.2.1 Qualitative analysis

In the preliminary laboratory experiments, we have conducted nine tests, with the parameters precises above. Figures 8.5 represent a typical results.The first figure shows the experiment after 21 s, the water has been injected at 8.6 $cm^3.s^{-1}$ from the injection area, where less dense water is injected with a small tube. This flow follows the domain's limit, and turn around the ridge. Two vortex areas are present, the first one just after the injection and the second one on the tip of the ridge. During the evolution of the flow, different behaviors are present. Initially, the injected flow follows the coast and turns around the ridge, where a β-plume forms. After a while, vortices fill up the injection area leading to a sea of eddies, that are about 1/4 of the ridge length, that is close to the predicted size. At the other side of the ridge, the β-plume crosses the basin and meets the coastal current there. Two distinct vortex paths are present,

a β-plume created on the tip of the ridge and the the coastal current. These are the essential features observed in the numerical simulations, which however show much more detail.
In view of time, I have not here to further explore this method and experiments.

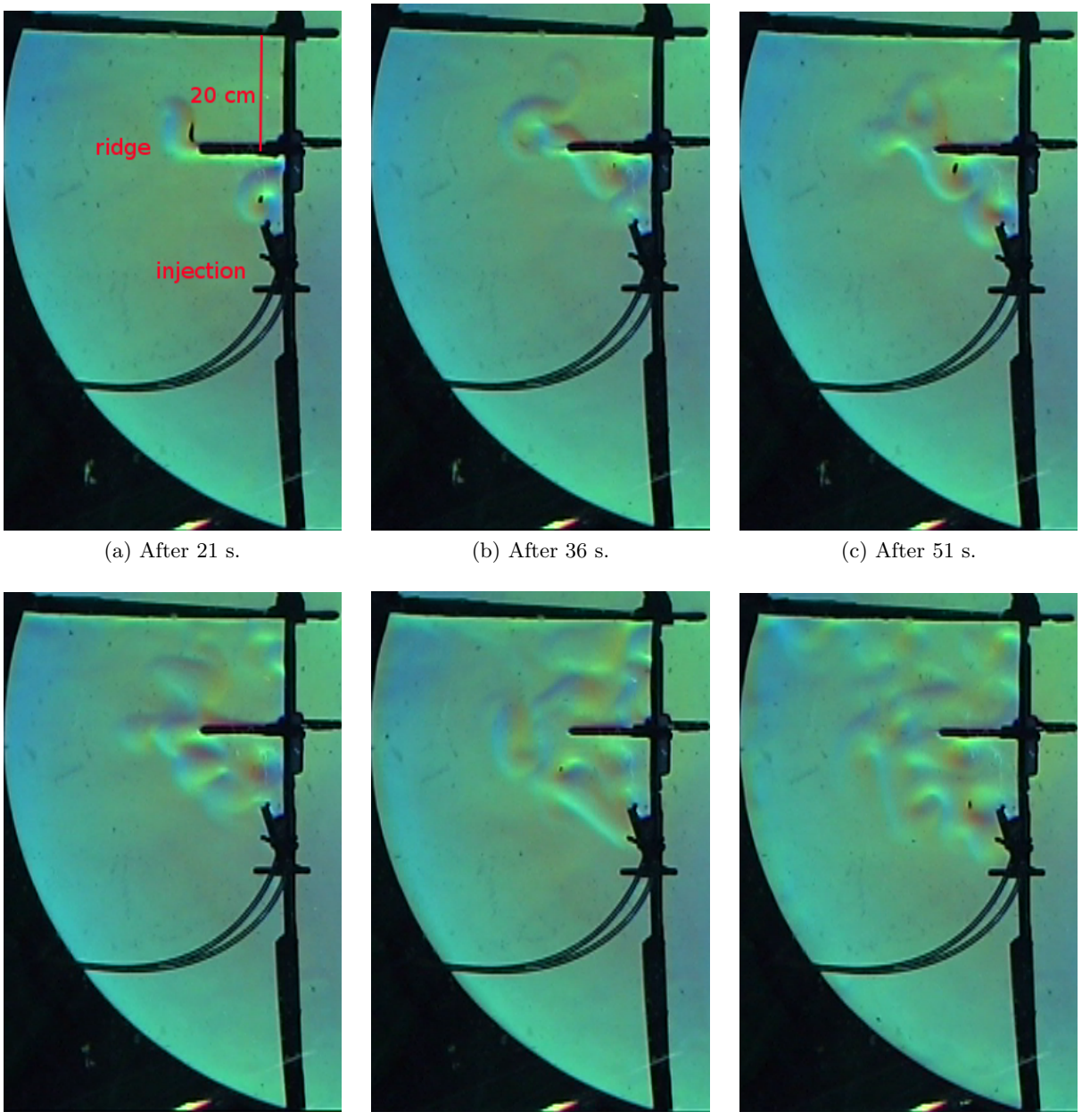

(a) After 21 s. (b) After 36 s. (c) After 51 s.

(d) After 71 s. (e) After 116 s. (f) After 166 s.

Figure 8.5: Laboratory observations of the Reykjanes ridge current, observe by the AIV method. Deformation radius $L_R = 3$ cm, Rossby number $Ro = 3 \times 10^{-2}$, $\Omega = 5.27$ rad.s^{-1}

Chapter 9

Discussion and prospectives

In this project, it is shown that for laminar and turbulent flows, a coastal current propagates along the iso-$\frac{f}{h}$ contours, turns around the ridge and follows the basin edges. For turbulent flows, there is an asymmetry between the two sides of the ridge, eddies are ejected from the ridge in the form of β-plumes. Along the ridge, large eddy structures evolve into smaller structures like filaments, before rolling up again into eddies.
This internship has been a first step to study the behavior of flows over the Reykjanes ridge and to construct and validate tools for PhD study. The numerical model and laboratory experiments have proved to be adapted to studying ridge flow.

The model can be improved on different points. First, bottom friction and a more realistic topography can be used in the model. Second, by using some numerical tools like parallelization, the resolution of the model can be refined. Laboratory experiments can be compared to the numerical simulations in detail allowing for further model improvements.

Bibliography

Afanasyev, Y., P. Rhines, and E. Lindahl, Vortices and rossby waves in cylinder wakes on a parabolic β-plane observed by altimetric imaging velocimetry, *Physics of Fluids (1994-present)*, *20*(8), 086,604, 2008.

Afanasyev, Y., P. Rhines, and E. Lindahl, Velocity and potential vorticity fields measured by altimetric imaging velocimetry in the rotating fluid, *Experiments in fluids*, *47*(6), 913–926, 2009.

Boffetta, G., and R. E. Ecke, Two-dimensional turbulence, *Annual Review of Fluid Mechanics*, *44*, 427–451, 2012.

Curry, R., and C. Mauritzen, Dilution of the northern north atlantic ocean in recent decades, *Science*, *308*(5729), 1772–1774, 2005.

Edwards, C. A., and J. Pedlosky, Dynamics of nonlinear cross-equatorial flow. part i: Potential vorticity transformation, *Journal of physical oceanography*, *28*(12), 2382–2406, 1998.

Poupart, E., *On the variability of the thermohaline circulation - Internship report*, 2011.

Sansón, L. Z., and G. Van Heijst, Interaction of barotropic vortices with coastal topography: Laboratory experiments and numerical simulations, *Journal of physical oceanography*, *30*(9), 2141–2162, 2000.

Thierry, V., and Y. Morel, Influence of a strong bottom slope on the evolution of a surface-intensified vortex, *Journal of physical oceanography*, *29*(5), 911–924, 1999.

Zhang, Y., and Y. Afanasyev, Beta-plane turbulence: experiments with altimetry, *arXiv preprint arXiv:1309.6197*, 2013.